ARTICLE IN PRESS

Available online at www.sciencedirect.com

ScienceDirect

Chemical Physics xxx (2007) xxx–xxx

Chemical Physics

www.elsevier.com/locate/chemphys

Imaging chemical interfaces perpendicular to the optical axis with focus-engineered coherent anti-Stokes Raman scattering microscopy

Vishnu Vardhan Krishnamachari *, Eric Olaf Potma

Department of Chemistry and Beckman Laser Institute, University of California at Irvine, Irvine, CA 92697, USA

Received 31 January 2007; accepted 7 June 2007

Abstract

In vibrational microscopy, it is often necessary to distinguish between chemically distinct microscopic objects and to highlight the "chemical interfaces" present in the sample under investigation. Here we apply the concept of focus engineering to enhance the sensitivity of coherent anti-Stokes Raman scattering (CARS) microscopy to these interfaces. Based on detailed numerical simulations, we show that using a focused Stokes field with a sharp phase jump along the longitudinal direction leads to the suppression of the signal from bulk regions and improves the signal contrast from vibrational resonant interfaces oriented perpendicular to the axis of beam propagation. We also demonstrate that the CARS spectral response from chemical interfaces exhibits a clean, Raman-like band-shape with such a phase-shaped excitation. This phenomenon of interface highlighting is a consequence of the coherent nature of CARS signal generation and it involves a complex interplay of the spectral phase of the sample and the spatial phase of the excitation fields.

PACS: 42.65.−k (Nonlinear optics); 42.65.Dr (CARS); 87.64.Vv (Multiphoton microscopy); 41.85.Ct (Beam shaping)

Keywords: Vibrational microscopy; Coherent anti-Stokes Raman scattering; Beam shaping; Interface detection

1. Introduction

CARS microscopy exhibits excellent sensitivity [1] and high chemical selectivity [2] to a variety of bio-molecular compounds and hence has been used as a non-invasive chemical imaging tool for analyzing biological cells and tissues [3–6]. On the engineering side, several signal generating and detecting configurations such as polarization-sensitive CARS [7], epi-CARS [8,9], heterodyne CARS [10] and frequency-modulation CARS [11] have been developed to reduce the deleterious effects of the non-resonant background in CARS images. Among these techniques, the epi-detection method is particularly attractive because of its experimental simplicity. The inherent large phase-mismatch in the epi-direction naturally suppresses the contribution from the bulk, while highlighting sub-wavelength objects as a result of incomplete destructive interference.

It was recently proposed that the suppression of the bulk contribution can be achieved even in the forward direction by employing CARS excitation profiles with alternative spatial phase distribution. In this approach, an engineered π-phase step is introduced in the excitation field so that the oscillators in one region of the focal volume are out of phase with respect to those from another region. For instance, the use of higher order Hermite–Gaussian focal Stokes fields enables the suppression of the homogeneous background while selectively highlighting "$\chi^{(3)}$-interfaces" or "chemical edges" [12]. It was also shown that the mere modification of the spatial phase of the excitation beams favorably influences the spectral characteristics of the CARS output. While the previous analysis was concerned with $\chi^{(3)}$-interfaces in the lateral plane, in the current work we investigate the possibility of detecting longitudinal $\chi^{(3)}$-interfaces – interfaces that are perpendicular to the

---

* Corresponding author. Tel.: +1 949 824 3374.
E-mail addresses: vishnuvk@uci.edu (V.V. Krishnamachari), epotma@uci.edu (E.O. Potma).

0301-0104/$ - see front matter © 2007 Elsevier B.V. All rights reserved.
doi:10.1016/j.chemphys.2007.06.004

Please cite this article in press as: V.V. Krishnamachari, E.O. Potma, Chem. Phys. (2007), doi:10.1016/j.chemphys.2007.06.004

direction of propagation of the beams – in the forward detection mode. The simplest way to detect longitudinal interfaces is to suppress the bulk signal from either side of the interface by engineering a CARS excitation focal field that undergoes a π-phase jump along the optical axis. To achieve this, we employ a Gaussian beam as the pump beam and an "optical bottle beam" as the Stokes beam for CARS signal generation.

An optical bottle beam has a dark focus surrounded by regions of higher intensity [13]. Such a beam shape has been effectively employed in generating optical traps for atoms [14]. Recently, it has found applications in light microscopy as well. For instance, in stimulated emission depletion (STED) microscopy [15–18], an optical bottle beam is utilized to quench the fluorescence in the regions above and below the plane of focus, which improves the resolution of fluorescence microscope substantially [19,20]. In addition to the unique focal intensity distribution, an optical bottle beam also exhibits an on-axis π-phase jump at the focus. This particular characteristic, which has received little attention so far, has important consequences in coherent techniques, such as CARS. In this article, we demonstrate, based on numerical simulation results, that the use of an optical bottle beam for the Stokes radiation in a CARS microscope setup enhances the signal sensitivity to longitudinal $\chi^{(3)}$-interfaces. This effect, analogous to the case of Hermite–Gaussian excitation [12], is a direct consequence of the coherent nature of CARS and can be explained by invoking the phenomenon of spatial interference among the CARS waves generated at various points in the excitation volume [21,22].

In the following section, we provide a qualitative description of the phase characteristics of an optical bottle beam and discuss how longitudinal $\chi^{(3)}$-interfaces can be detected when such a field is employed in a typical CARS setup. In Section 3, we review the basic vectorial theory of beam focusing, CARS excitation field generation and far-field intensity detection. In Section 4, we present the numerical results and compare the CARS radiation patterns, CARS intensity line scans of longitudinal interfaces, and the spectral dependence of the CARS output under conventional and optical bottle beam excitations. We also show that the intensity profiles obtained by scanning the CARS excitation across longitudinal edges display a strong dependence on the orientation of the interface.

2. Optical bottle beam and CARS microscopy – a qualitative discussion

There are two ways of generating an optical bottle beam: (a) by diffraction from an appropriately designed hologram [13] or (b) by employing a binary phase plate with the central portion of the plate being π-phase shifted with respect to that of the outer portion [14] (see Fig. 1). Focusing a beam that is diffracted from or transmitted through either of these phase plates generates a dark focus surrounded by regions of higher intensity. The holographic technique leads to steeper intensity gradients in the lateral plane and hence is preferred in applications involving optical beam traps. On the other hand, a binary phase plate is experimentally simpler to realize and its corresponding focal field distribution is mathematically easier to model. Hence, in this article, we choose the binary phase plate for generating an optical bottle beam. A typical experimental configuration is shown in Fig. 1.

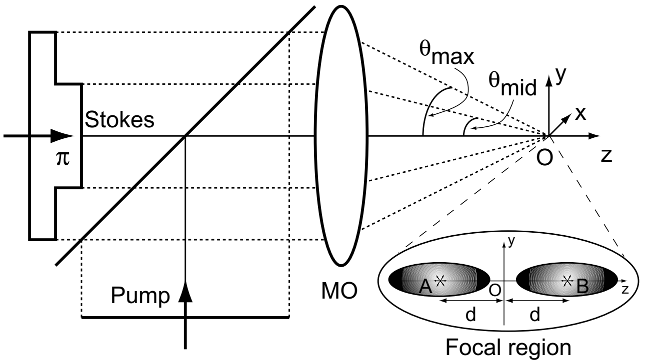

Fig. 1. Sketch depicting the binary phase plate configuration to generate an optical bottle beam. The optical bottle beam excitation in CARS microscopy is obtained by using a Stokes beam with bottle beam field distribution and a pump beam with a Gaussian wavefront. The inset shows a representative sketch of the double-humped intensity distribution in the focal volume; the two intensity humps are out-of-phase by π-radians.

The three-dimensional vectorial focal amplitude distribution of arbitrary input fields can be calculated based on the angular spectrum formalism introduced by Richards and Wolf [23]. Figs. 2a and b show the *x*–*z* intensity cross section of the *x*-polarization of a focused Gaussian input wave front and a focused phase aberrated (bottle beam) input wavefront using a high numerical aperture objective with an acceptance angle of $\theta_{\max} = 60°$ (corresponding to a numerical aperture of 1.1 for water-immersion objective). The half-angle subtended by the π-shifted portion of the phase plate at the focal plane is calculated to be $\theta_{\text{mid}} \approx 38.02°$ [24]. This leads to zero on-axis intensity for the optical bottle beam as shown in Fig. 2b. The corresponding on-axis phase profiles after subtracting the linear phase of propagation are plotted in Fig. 2c and d. Fig. 2e shows the phase variation at the focal region of the optical bottle beam along the optical axis after subtracting the linear phase and the Gouy phase shift. Clearly, there appears a π-phase discontinuity at the focal plane, which ensures that the portions of the focused field above and below the plane of focus are out-of-phase with respect to each other.

CARS is a third-order nonlinear process in which two photons of a pump beam of angular frequency ω_p and a photon of a Stokes beam with angular frequency ω_S interact with the third-order susceptibility, $\chi^{(3)}(-\omega_{as}; \omega_p, \omega_p, -\omega_S)$, of the medium to generate an anti-Stokes photon at an angular frequency of $\omega_{as} = 2\omega_p - \omega_S$. The anti-Stokes signal is enhanced if the frequencies of the pump and the Stokes beams are such that their difference

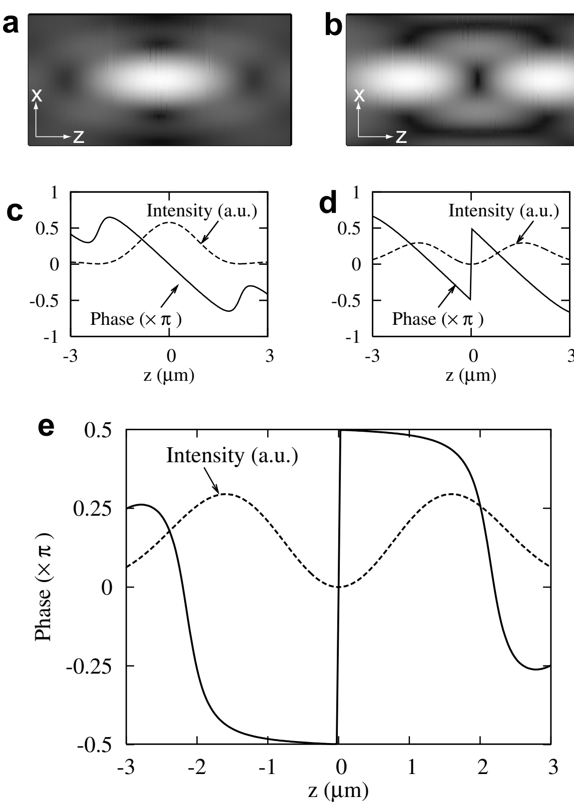

Fig. 2. The x component of the focal field intensity of (a) a Gaussian beam and (b) an optical bottle beam and the on-axis phase after subtracting the linear propagation phase of (c) a Gaussian beam and (d) an optical bottle beam. For clarity, the on-axis intensity profiles of the corresponding beams are plotted in (c) and (d) in arbitrary units. (e) Plot of residual phase, obtained by subtracting the phase profile shown in Fig. (c) from that in Fig. (d), as a function of the longitudinal coordinate. The dotted line corresponds to the on-axis intensity profile of the optical bottle beam in arbitrary units. The calculations correspond to the Stokes wavelength of 1064 nm.

($\omega_p - \omega_S$) is equal to a vibrational transition, ω_R, of the medium. The phase, ϕ_{as}, of the emitted anti-Stokes signal is intricately related to the phases of the incident pump and the Stokes beams through the expression $\phi_{as} = 2\phi_p - \phi_S$.

If the input Stokes beam is an optical bottle beam, then the emitted CARS signals from either side of the focal plane are out-of-phase by π-radians. Note that this phase difference is the residual phase discontinuity after taking into account the accumulated phase due to linear propagation and the Gouy phase shift. As a consequence, the forward propagating CARS signal from the bulk is significantly reduced, due to destructive interference among the signals generated from the regions above and below the focal plane. However, in the presence of an interface in the excitation volume, the destructive interference is offset, leading to a non-zero forward propagating signal. This phenomenon of incomplete destructive interference is most prominent when the medium on one side of the interface is vibrationally resonant, because the resonant spectral phase cancels out the engineered phase shift of the excitation field. The objective of this article is to investigate this phenomenon of longitudinal interface highlighting in forward CARS.

3. Optical bottle beam and CARS microscopy – theoretical description

The general theory of CARS generation, field propagation, and net CARS intensity detection using high numerical aperture objectives has been discussed in the literature [21,22]. Our calculations follow the angular spectrum approach introduced by Richards and Wolf [23]. Based on the numerical strategy presented in Ref. [12], we assume no index mismatch [25] and neglect linear dispersion. Following the approach used by Novotny and Hecht [26], the focal field of a bottle beam can be written to within a complex multiplicative factor as

$$\mathbf{E}(\rho,z) = \mathrm{e}^{\mathrm{i}\pi}\begin{pmatrix} I_{00}^{(1)} + I_{02}^{(1)}\cos 2\phi \\ I_{02}^{(1)}\sin 2\phi \\ -2\mathrm{i}I_{01}^{(1)}\cos\phi \end{pmatrix} + \begin{pmatrix} I_{00}^{(2)} + I_{02}^{(2)}\cos 2\phi \\ I_{02}^{(2)}\sin 2\phi \\ -2\mathrm{i}I_{01}^{(2)}\cos\phi \end{pmatrix} \tag{1}$$

In the above equation, x, y and z are the cartesian coordinates with the coordinate origin at the focal plane on the optical axis, ϕ is the azimuthal angle, $\rho = \sqrt{x^2+y^2}$, and the quantities $I_{mn}^{(p)}, (p = 1,2; m = 0,1; n = 0,\ldots,4)$ are one-dimensional integrals with respect to the polar angle, θ, and are given by

$$I_{mn}^{(p)}(\rho,z) = \int_{a_p}^{b_p} f_w(\theta)\sqrt{\cos\theta}\,g_{mn}(\theta)J_l(k\rho\sin\theta)\mathrm{e}^{\mathrm{i}kz\cos\theta}\sin\theta\,\mathrm{d}\theta \tag{2}$$

where J_l's are Bessel functions of the first kind, k is the amplitude of the wave-vector of the field and $f_w(\theta)$ is the apodization function which is equal to one (corresponding to complete illumination of the entrance pupil of the objective). The function $g_{mn}(\theta)$ and the indices m, n and l are related as follows: $l = n$ if $n \leqslant m$, and $l = n - m$ if $n > m$ and $g_{0n} = 1+\cos\theta,\ \sin\theta,\ 1-\cos\theta$ for $n = 0,1,2$ and $g_{1n} = \sin^2\theta,\ \sin\theta(1+3\cos\theta),\ \sin\theta(1-\cos\theta),\ \sin^2\theta,\ \sin\theta(1-\cos\theta)$ for $n = 0,1,2,3,4$, respectively. The limits of integration are $a_1 = 0$, $b_1 = a_2 = \theta_{mid}$, and $b_2 = \theta_{max}$. The first term on the right-hand side in Eq. (1) corresponds to the contribution of the π-phase shifted central portion of the phase plate and the second term corresponds to that of the 0°-phase shifted annular outer region of the phase plate. To account for the case when there is no phase plate in the input Gaussian beam, the π-phase factor in the first term on the right-hand side is set to 0°.

The induced nonlinear polarization density, $\mathbf{P}_{as}(\mathbf{r})$, in the material at the CARS wavelength can be written as

$$P_{asi}(\mathbf{r}) = \sum_{j,k,l}\chi_{ijkl}^{(3)}(\mathbf{r})E_{pj}(\mathbf{r})E_{pk}(\mathbf{r})E_{Sl}^{*}(\mathbf{r}) \tag{3}$$

where $\mathbf{E}_p$ and $\mathbf{E}_S$ correspond to the focal fields of the pump and the Stokes beams, respectively, and $\chi^{(3)}$ is the third-order nonlinear susceptibility tensor of the medium. The ele-

Please cite this article in press as: V.V. Krishnamachari, E.O. Potma, Chem. Phys. (2007), doi:10.1016/j.chemphys.2007.06.004

ments of the susceptibility tensor can be written as a sum of resonant (χ_{ijkl}^{R}) and non-resonant (χ_{ijkl}^{NR}) contributions: $\chi_{ijkl}^{(3)} = \chi_{ijkl}^{R} + \chi_{ijkl}^{NR}$. These tensor elements can be expressed in terms of a single component [27]:

$$\chi_{ijkl}^{R,NR} = \chi_{xxxx}^{R,NR}\left(\delta_{ij}\delta_{kl} + \delta_{ik}\delta_{jl} + \frac{2\rho_{CARS}^{R,NR}}{1-\rho_{CARS}^{R,NR}}\delta_{il}\delta_{jk}\right)\rho_{CARS}^{R,NR} \tag{4}$$

where

$$\rho_{CARS}^{R,NR} \equiv \frac{\chi_{ijji}^{R,NR}}{\chi_{iiii}^{R,NR}} = \frac{\chi_{ijji}^{R,NR}}{(\chi_{ijji}^{R,NR} + 2\chi_{ijij}^{R,NR})} \tag{5}$$

are the resonant/non-resonant CARS depolarization ratios. Under the assumption of no electronic resonances, the non-resonant depolarization ratio, $\rho_{CARS}^{NR} = 1/3$. However, the resonant depolarization ratio lies between 0 and 0.75. Without any loss of generality, we assume that $\rho_{CARS}^{R} = 1/3$ which implies the Raman modes that are being investigated are isotropic. This assumption does not change the physics of the phenomenon being described below. (A more detailed study of the influence of Raman depolarization ratio on the CARS output can be found in Ref. [27].) Hence, considering a sample with a single vibrational resonance, $\chi_{xxxx}^{(3)}$ can be expressed as

$$\chi_{xxxx}^{(3)} = \chi_{nr} + \frac{\mathscr{G}}{\omega_p - \omega_S - \omega_R + i\Gamma_R} \tag{6}$$

where the first term is the vibrationally non-specific, electronic background contribution and is assumed to be constant in the spectral range of interest. The second term is the resonant contribution consisting of a vibrational resonance at the angular frequency ω_R with a transition half-width of $\Gamma = 10\ \text{cm}^{-1}$. The factor $\mathscr{G}$ is chosen such that at resonance (*i.e.* $\omega_p - \omega_S = \omega_R$), the resonant amplitude contribution is 2.5 times the non-resonant contribution.

The nonlinear polarization density generated in the medium due to the focusing of the pump and the Stokes beams can be considered as a collection of coherent dipoles radiating at angular frequency $\omega_{as} = 2\omega_p - \omega_S$. The resulting radiation intensity at any far-field coordinate point, $\mathbf{R}$, is obtained by integrating the propagating fields from all these dipoles:

$$\mathbf{E}(\mathbf{R}) = -\int_{\mathscr{V}} \frac{e^{ik_{as}|\mathbf{R}-\mathbf{r}|}}{4\pi|\mathbf{R}-\mathbf{r}|^3}(\mathbf{R}-\mathbf{r}) \times [(\mathbf{R}-\mathbf{r}) \times \mathbf{P}_{as}(\mathbf{r})]d^3\mathbf{r} \tag{7}$$

where k_{as} is the magnitude of the wave-vector of the CARS signal. The forward CARS intensity profile is generated by summing the far-field CARS intensity within the acceptance angle of the collecting lens system.

4. Longitudinal interface detection: numerical results

Assuming the wavelengths of the pump and the Stokes beams to be 800 nm and 1064 nm, respectively, and that both the beams are initially polarized along the x-direction, the focal field distributions of the individual fields, the induced CARS polarization density and the far-field CARS intensity are derived using Eqs. (1)–(7). To provide a better appreciation of the effects due to longitudinal phase shaping, we compare all the results using optical bottle beam excitation (where the input pump beam is Gaussian and the Stokes beam is a bottle beam) with those obtained employing conventional excitation (where the input pump and the Stokes beams are Gaussian). Figs. 3a and b show the x-component of the CARS polarization density under both the excitations in the presence of a bulk non-resonant medium. The phase profile of the CARS polarization density (see Fig. 3c) clearly shows a π-phase discontinuity at the plane of focus – a direct consequence of the engineered phase jump in the Stokes beam. Thus the signals emanating from any two points such as A and B (shown in the inset of Fig. 1) which are equidistant from the focal plane, would interfere destructively at a far-field point along the optical axis.

In the following sections, we provide numerical results of detecting simple longitudinal interfaces depicted in Fig. 4a–c. In particular, we investigate the CARS radiation pattern and the intensity profiles along the edges $\mathfrak{I}_1$ (Fig. 4a) and $\mathfrak{I}_2$ (Fig. 4b) formed between a resonant medium and a non-resonant bulk whose third-order nonlinear susceptibilities are χ_1 and χ_2, respectively. Note the only difference between these two interfaces is their orientation: the former corresponds to a resonant-to-non-resonant transition and the latter corresponds to a non-resonant-to-resonant transition. We also briefly consider the situation in which a layer of the resonant medium is sandwiched

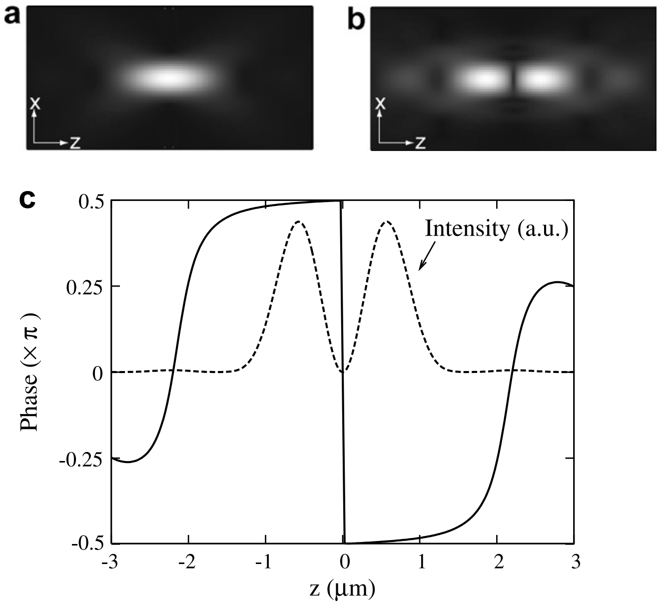

Fig. 3. The x–z cross section of the x component of the amplitude of the focal CARS polarization in the presence of a non-resonant bulk with (a) Gaussian excitation and (b) optical bottle beam excitation. (c) Plot of the on-axis residual phase discontinuity in the CARS polarization under OBB excitation as a function of the longitudinal coordinate. The dotted line corresponds to the on-axis CARS polarization amplitude plotted in arbitrary units.

Please cite this article in press as: V.V. Krishnamachari, E.O. Potma, Chem. Phys. (2007), doi:10.1016/j.chemphys.2007.06.004

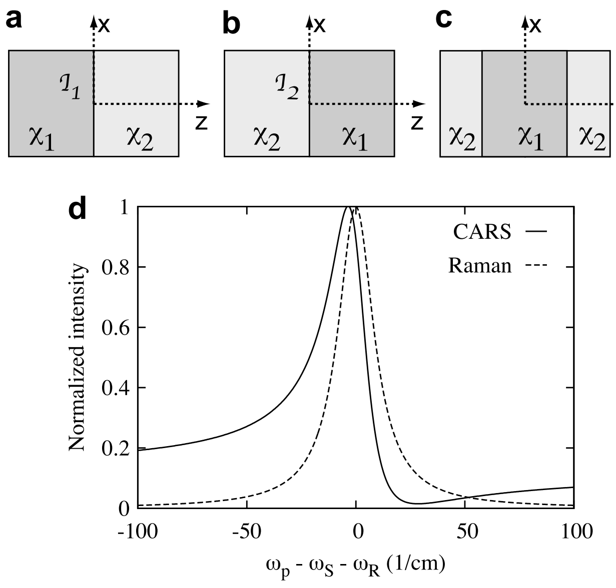

Fig. 4. Sketch of the longitudinal interfaces being investigated: (a) resonant to non-resonant interface, denoted as $\Im_1$ (b) non-resonant to resonant interface, denoted as $\Im_2$ and (c) double interface with the resonant medium being sandwiched between the non-resonant medium; the thickness of the resonant medium is 1.5 μm. χ_1 and χ_2 are the third-order nonlinear susceptibilities of the resonant and the non-resonant media respectively. (d) Assumed spectral dependence of χ_1 – the solid curve: CARS spectrum, and the dashed curve: Raman spectrum.

between the non-resonant bulk (Fig. 4c). Regarding the susceptibility, χ_1, of the resonant medium, we make the following two assumptions: (a) the non-resonant part of χ_1 is equal to χ_2 and (b) the excitation frequency is at resonance, *i.e.* $\omega_R = \omega_p - \omega_S = 3101.5\ \mathrm{cm}^{-1}$ except in Section 4.4 where we discuss the spectral dependence of the CARS output. With these assumptions, we plot the Raman and the CARS spectral dependence of χ_1 in Fig. 4d.

4.1. CARS radiation pattern

Before considering the longitudinal interface detection, we first compare the far-field CARS radiation patterns from the bulk under conventional and OBB excitations. Fig. 5a shows the well-known angular dependence of the far-field CARS intensity from the bulk using conventional excitation. Along the optical axis ($\theta = 0°$), the CARS waves emanating from different points in the focal volume interfere constructively. On the other hand for larger angles, due to varied optical path lengths traversed by these signals, the condition for constructive interference is no longer optimal and hence the far-field CARS intensity gradually reduces.

Fig. 5b shows the influence of OBB excitation on the radiation pattern. Note that the intensity along the optical axis is negligibly small in contrast to the case of conventional excitation. This can be explained by invoking the coherent nature of the CARS field. Let us consider two points A and B (as shown in the inset of Fig. 1) along the optical axis that are located at equal distances on either side of the plane of focus. Under OBB excitation, the CARS signals generated at these points are not in phase. Though the actual value of the phase difference varies with the location of the points with respect to the focal plane (as indicated in Fig. 3c), it is approximately equal to π-radians. Once again we emphasize that this phase difference is the residual phase shift after subtracting the Gouy phase shift and the linear phase. Hence, at any far-field point along the optical axis, these two signals interfere (almost) destructively. However, for non-zero polar angles, the destructive interference is not as complete due to unequal optical path lengths traversed by the waves from the points A and B. As a consequence, for larger angles the detected CARS signal is more intense and it reaches a maximum at an angle at which the optical path length difference compensates for the phase shift introduced by longitudinal phase shaping. A second aspect that is evident in this radiation pattern is that it is not rotationally symmetric about the optical axis. This arises because of the particular choice of the incident x polarization of the beams. By integrating the far-field intensity over the cone angle of the detection aperture (which is assumed to be 10° as depicted in Fig. 5b), the net CARS intensity is obtained for a given position of the sample with respect to the excitation volume. Thus

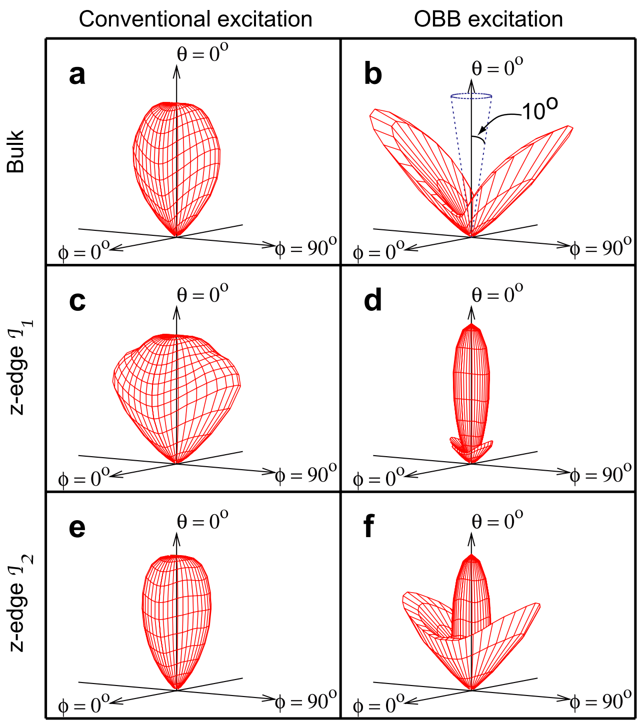

Fig. 5. Comparing the far-field CARS radiation pattern from the bulk: (a) and (b); the $\Im_1$ interface: (c) and (d); and the $\Im_2$ interface: (e) and (f) under conventional excitation (left column) and OBB excitation (right column). θ and ϕ are the polar and the azimuthal angles, respectively. The directions $\phi = 0$ and $\phi = 90°$ correspond to positive x and y directions. The acceptance angle of detection is 10° and is indicated in (b). The absolute values of the far-field intensity pattern under OBB excitation is generally lower than that under conventional excitation. The scaling factors of the radiation patterns under OBB excitation for the bulk, the $\Im_1$ interface and the $\Im_2$ interface are 26.7, 5.6 and 22.2, respectively.

under OBB excitation, the net CARS intensity from a homogeneous medium is negligibly small even though the medium could be highly resonant.

Figs. 5c and e show the far-field CARS radiation patterns under conventional excitation in the presence of the interfaces $\Im_1$ and $\Im_2$, respectively. Though these patterns are different in shape compared to that of bulk radiation, they still show the essential feature of stronger CARS intensity along the optical axis. On switching to OBB excitation, the radiation patterns (Fig. 5d and f) from the interfaces are significantly different. Most importantly, the intensity along the optical axis is stronger compared to the off-axis points. This is a direct consequence of incomplete destructive interference among the signals from the points such as A and B due to the presence of two spectroscopically different materials across the focal plane. Hence the net CARS intensity obtained by integrating over the cone of the detection aperture is stronger. Consequently, under OBB excitation, as the focal spot is scanned across the sample along the z-direction, a strong net CARS signal is expected whenever a longitudinal $\chi^{(3)}$-interface is encountered in the excitation volume.

A careful examination of the two sets of radiation patterns shown in Figs. 5c and e, and 5d and f reveals one of the interesting aspects of CARS imaging – the directional dependence. These different patterns are obtained from identical interfaces with only their sense of orientation being opposite. This clearly demonstrates that the CARS signals from the focal volume add up differently for different orientations of the sample and it emphasizes the complex nature of CARS signal generation in which the phases of the optical beams are intricately coupled to the spectral phase of the sample. This asymmetry and the directional dependence of the CARS output disappears if the media on either side of the interface are both non-resonant.

4.2. Line scan of an edge

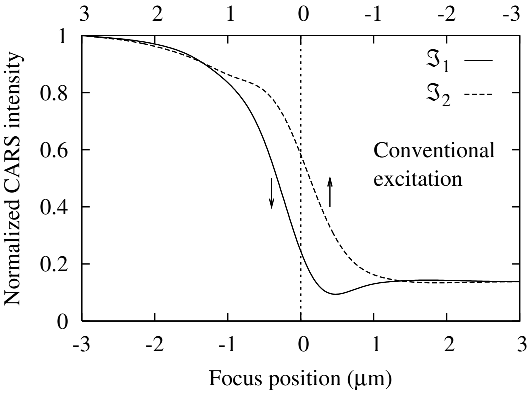

Fig. 6. Far-field CARS intensity profiles obtained by scanning the conventional excitation spot along the z-direction across the $\Im_1$ (solid curve) and $\Im_2$ (dashed curve) interfaces. Note the different assignments of abscissae.

Fig. 6 compares the z-intensity scan across $\Im_1$ and $\Im_2$ interfaces under conventional excitation. In both the curves, the net CARS intensity in the region of the resonant medium is larger and gradually reduces to a lower value in the region of the non-resonant bulk. However, as discussed in the previous section, even under conventional excitation the directional dependence of the CARS output is obvious in the profiles of the two curves. The curve corresponding to $\Im_1$ interface – resonant to non-resonant transition – has a lower value at the $\chi^{(3)}$-discontinuity and also exhibits a dip around $z = 0.47$ μm. This dependence on the interface orientation vanishes when the frequency difference of the pump and Stokes approaches zero. This effect also diminishes when lower numerical aperture lenses are used for focusing the incident beams. These observations suggest a prominent role of the Gouy phase mismatch defined as $\Delta\phi_g \equiv |\phi^g_{as} - 2\phi^g_p + \phi^g_S|$, where ϕ^g_p, ϕ^g_S and ϕ^g_{as} are the Gouy phases of the pump, the Stokes and the CARS beams, respectively. The propagation direction of the pump and the Stokes beam imposes a directional dependence on the net CARS signal generation process through the unambiguous Gouy phase jump in the individual beams. Hence, the generated CARS waves in the focal volume add up differently depending on whether the excitation beams encounter the resonant material before the non-resonant medium or vice-versa. Note that the Gouy phase mismatch is zero only when the frequencies of the incoming beams are identical or when the incident beams are plane parallel waves.

Fig. 7 shows the equivalent intensity line scans under OBB excitation for the two interfaces. Though the absolute output intensity is lower by an order of magnitude, the profiles of the line scan show significant differences from the conventional case. The most evident features are (a) the curves peak near the interface, (b) the CARS output in the homogeneous regions is suppressed, and (c) the curves are asymmetric about the $\chi^{(3)}$-discontinuity. The first two effects, as explained in the previous sections is a consequence of spatial interference among the signal waves

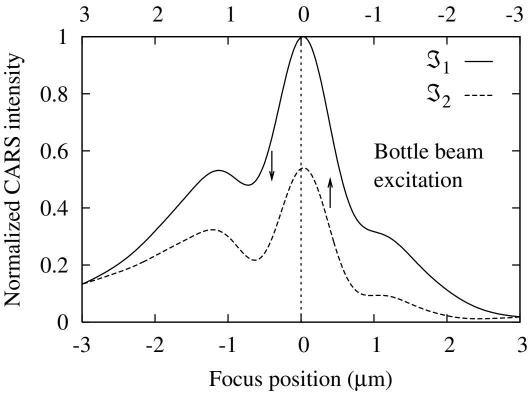

Fig. 7. Far-field CARS intensity profiles obtained by scanning the OBB excitation spot along the z-direction across the $\Im_1$ (solid curve) and $\Im_2$ (dashed curve) interfaces. Note the different assignments of abscissae. The intensity profiles in this figure are scaled by a factor of 23.3 with respect to those in Fig. 6.

Please cite this article in press as: V.V. Krishnamachari, E.O. Potma, Chem. Phys. (2007), doi:10.1016/j.chemphys.2007.06.004

generated in the focal volume. The asymmetry in the profiles emphasizes the directional dependence of CARS signal generation. For good imaging contrast of the interface with OBB excitation, ideally the intensity away from the interface should be negligibly small. However with the current choice of longitudinal phase step, as shown in Fig. 2e, the phase jump introduced due to the spatial phase shaping gradually reduces from π-radians away from the focal plane and hence leads to non-zero intensity in the regions away from the interface. Comparing the curves in Figs. 6 and 7, it is seen that the intensity ratio between the curves at $z = 0$ corresponding to the two interfaces is reversed – under conventional excitation, the output from the $\Im_1$ interface is stronger whereas under OBB excitation, the intensity from $\Im_2$ interface is stronger.

4.3. CARS image of a double-edge

Fig. 8a shows the simulated x–z CARS image of the double-edge depicted in Fig. 4c under conventional excitation. As expected, the central resonant region of the sample is brighter compared to the outer non-resonant regions. For convenience, the location of the $\chi^{(3)}$-edges are indicated with dashed lines. Note the asymmetry in the intensity variation – at the non-resonant to resonant interface the transition from darkness to brightness is smooth whereas at the resonant to non-resonant interface, the intensity drops down abruptly. The corresponding CARS image under OBB excitation is shown in Fig. 8b. Clearly the output intensity at interfaces is larger; the bulk information from both the resonant and the non-resonant regions is suppressed. Once again, we notice the difference in the output intensity at the two interfaces. As indicated in Fig. 7, the output intensity is about two times larger at the resonant to non-resonant transition. This directional dependence can be used to characterize the nature of $\chi^{(3)}$ interfaces and thus to discriminate a resonant-to-non-resonant transition from a non-resonant-to-resonant transition.

In this context it is important to discuss the advantages or disadvantages of the technique of longitudinal interface detection by spatial phase shaping and interface detection using the epi-CARS detection scheme. Epi-CARS, similar to the technique discussed here, highlights sub-wavelength sized $\chi^{(3)}$ inhomogeneities by suppressing the bulk information. However, in turbid samples the detected the epi-signal is contaminated with strongly backward reflected forward CARS signal and thus it is very difficult to distinguish the origin of the detected output intensity. On the contrary, the current technique of longitudinal phase shaping does not suffer from this problem; here, the longitudinal interface information is detected in the forward direction and the origin of this forward-propagating signal is well-defined. Although systematic experimental investigations are required to provide a quantitative comparison between the two techniques, at least from a theoretical point of view it is evident that the current technique offers interface information devoid of spurious signals.

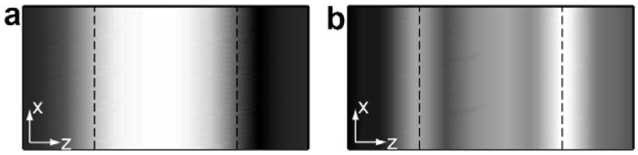

Fig. 8. The x–z CARS images of the double-edge: (a) with conventional excitation and (b) with OBB excitation. The image size is 3 μm along x-direction and 6 μm along z-direction. The thin dotted lines indicate the location of the interface. The CARS image under OBB excitation is about 20 times weaker in intensity than that under conventional excitation.

4.4. Spectral dependence

To investigate the spectral dependence of the CARS output from interfaces, we vary the resonance frequency ω_R of the resonant medium by keeping the excitation frequency, $\omega_{ex} = \omega_p - \omega_S$, constant. By choosing a constant ω_{ex}, we avoid the effects of focal spot variations (which are less than 1% in the desired spectral range of $\pm 100\ \mathrm{cm}^{-1}$) due to changes in the wavelengths of the pump or the Stokes beams. This enables us to focus only on the effects originating from the spectral characteristics of the sample. Fig. 9 compares the spectral variation of the far-field CARS intensity from longitudinal interfaces $\Im_1$ and $\Im_2$ under conventional and OBB excitations obtained by fixing the CARS excitation volume at the interface. The spectral variation of the CARS output from either interface exhibits dispersive behavior under conventional excitation. On switching to OBB excitation, the output from both interfaces are Lorentzian-like and closely resemble the Raman spectrum of the resonant medium as shown in Fig. 4d. The difference in the output intensities from $\Im_1$ and $\Im_2$, arises due to different ways in which the signals add up at a far-field point. This Lorentzian-like result, analogous to that described in Ref. [12], clearly demonstrates that spatial phase shaping, apart from interface highlighting, can be used as a versatile technique for

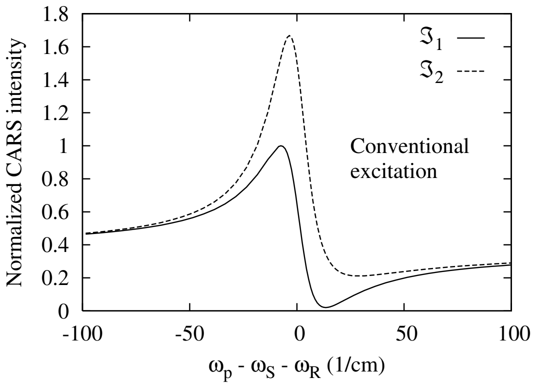

Fig. 9. Spectral dependence of the far-field CARS output from $\Im_1$ (solid curve) and $\Im_2$ (dashed curve) obtained under conventional excitation. The curves are normalized with respect to the maximum of the solid curve.

Please cite this article in press as: V.V. Krishnamachari, E.O. Potma, Chem. Phys. (2007), doi:10.1016/j.chemphys.2007.06.004

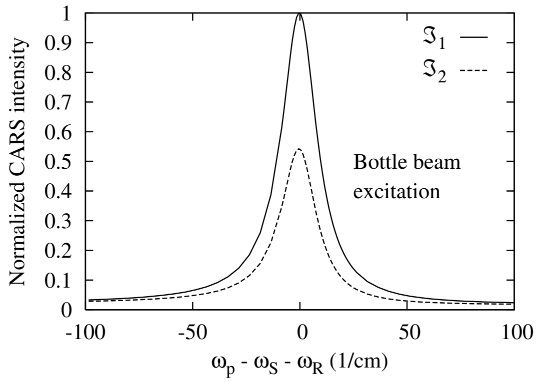

Fig. 10. Spectral dependence of the far-field CARS output from $\Im_1$ (solid curve) and $\Im_2$ (dashed curve) obtained under OBB excitation. The curves are normalized with respect to the maximum of the solid curve. Note that the intensity profiles in this figure are scaled by a factor of 8.8 with respect to those in Fig. 9.

improving the spectral characteristics of the CARS output (see Fig. 10).

5. Conclusion

In this article, we applied the concept of focus engineering in narrowband CARS microscopy to detect chemical interfaces in the longitudinal direction. By employing an optical bottle beam as the Stokes radiation field, we demonstrated, based on qualitative arguments and rigorous numerical simulations, that it is possible to highlight $\chi^{(3)}$-interfaces that are perpendicular to the direction of beam propagation. We also showed that the radiation patterns and the intensity line scans of the CARS output are different depending on whether the excitation beams propagate from a resonant to a non-resonant medium or vice versa. We compared the spectral dependence of the CARS output under both conventional and optical bottle beam excitations and established that the spectral characteristics of the CARS output can be improved by the spatial phase shaping technique.

The results and the discussions presented in this article clearly bring forward the complex interplay of the spectral phase of the sample and the spatial phase of the excitation fields. Though the analysis presented here pertains to simple and ideal interfaces with the assumptions of no index mismatch and zero linear dispersion, we believe that employing the technique of focus engineering in various coherent nonlinear microscopic techniques holds considerable potential for providing useful insights about the chemical and/or the structural properties of the sample and can complement those obtained under conventional excitation.

References

[1] E.O. Potma, X.S. Xie, J. Raman Spectrosc. 34 (2003) 642.
[2] C. Otto, A. Voroshilov, S.G. Kruglik, J. Greve, J. Raman Spectrosc. 32 (2001) 495.
[3] J.-X. Cheng, X.S. Xie, J. Phys. Chem. B 108 (2004) 827.
[4] C.L. Evans, E.O. Potma, M. Puoris'haag, D. Côté, C.P. Lin, X.S. Xie, Proc. Natl. Acad. Sci. 102 (2005) 16807.
[5] H. Wang, Y. Fu, P. Zickmund, R. Shi, J.-X. Cheng, Biophys. J. 89 (2005) 581.
[6] X. Nan, E.O. Potma, X.S. Xie, Biophys. J. 91 (2006) 728.
[7] J.-X. Cheng, L.D. Book, X.S. Xie, Opt. Lett. 26 (2001) 1341.
[8] J.-X. Cheng, A. Volkmer, L.D. Book, X.S. Xie, J. Phys. Chem. B 1057 (2001) 1277.
[9] A. Volkmer, J.-X. Cheng, X.S. Xie, Phys. Rev. Lett. 87 (2001) 023901.
[10] E.O. Potma, C.L. Evans, X.S. Xie, Opt. Lett. 31 (2006) 241.
[11] F. Ganikhanov, C.L. Evans, B.G. Saar, X.S. Xie, Opt. Lett. 31 (2006) 1872.
[12] V.V. Krishnamachari, E.O. Potma, J. Opt. Soc. Am. A 24 (2007) 1138.
[13] J. Artl, M.J. Padgett, Opt. Lett. 25 (2000) 191.
[14] R. Ozeri, L. Khaykovich, N. Davidson, Phys. Rev. A 59 (1999) R1750.
[15] S. Hell, J. Wichmann, Opt. Lett. 19 (1994) 780.
[16] T.A. Klar, S. Hell, Opt. Lett. 24 (1999) 954.
[17] S.W. Hell, E.H.K. Stelzer, Opt. Commun. 93 (1992) 277.
[18] A. Egner, S. Jakobs, S.W. Hell, Proc. Natl. Acad. Sci. 99 (2002) 3370.
[19] T.A. Klar, S. Jakobs, M. Dyba, A. Egner, S. Hell, Proc. Natl. Acad. Sci. 97 (2000) 8206.
[20] M. Dyba, S.W. Hell, Phys. Rev. Lett. 88 (2002) 163901.
[21] E.O. Potma, W.P. de Boeij, D.A. Wiersma, J. Opt. Soc. Am. B 17 (2000) 1678.
[22] J.-X. Cheng, A. Volkmer, X.S. Xie, J. Opt. Soc. Am. B 19 (2002) 1363.
[23] B. Richards, E. Wolf, Proc. Roy. Soc. A 253 (1959) 358.
[24] Assuming the input beams fill the input aperture of the objective, the angle θ_{mid} can be calculated as function of the acceptance angle (or the NA) of the objective. The result is obtained by solving the following algebraic equation obtained by integrating the focal integrals at the origin and equating the resulting expression to zero: $10x^{3/2} + 6x^{5/2} - 5b^{3/2} - 3b^{5/2} - 8 = 0$ where $x = \cos\theta_{\mathrm{mid}}$ and $b = \cos\theta_{\mathrm{max}}$.
[25] We assume no refractive index mismatch so as to disentangle the effects of $\chi^{(3)}$ differences from $\chi^{(1)}$ differences. This we believe would provide a better appreciation of the effects of unconventional spatial excitation on the output of a coherent process such as CARS.
[26] L. Novotny, B. Hecht, Principles of Nano-optics, Cambridge University Press, New York, 2006.
[27] D. Gachet, N. Sandeau, H. Rigneault, JEOS:RP 1 (2006) 06013.

Please cite this article in press as: V.V. Krishnamachari, E.O. Potma, Chem. Phys. (2007), doi:10.1016/j.chemphys.2007.06.004